

1 **Tropopause Evolution in a Rapidly Intensifying Tropical Cyclone: A Static**
2 **Stability Budget Analysis in an Idealized, Axisymmetric Framework**

3 Patrick Duran* and John Molinari

4 *University at Albany, State University of New York, Albany, NY*

5 **Corresponding author address:* Department of Atmospheric and Environmental Sciences, Univer-
6 sity at Albany, State University of New York, 1400 Washington Avenue, Albany, NY.

7 E-mail: pduran2008@gmail.com

ABSTRACT

8 Large changes in tropopause-layer static stability are observed during the
9 rapid intensification (RI) of an idealized, axisymmetric tropical cyclone (TC).
10 Over the eye, static stability near the tropopause decreases and the cold-point
11 tropopause height rises by up to 4 km at the storm center. Outside of the eye,
12 static stability increases considerably just above the cold-point tropopause,
13 and the tropopause remains near its initial level.

14 A budget analysis reveals that the advection term, which includes differen-
15 tial advection of potential temperature and direct advection of static stability,
16 is important throughout the upper troposphere and lower stratosphere. Within
17 the eye, differential advection plays a particularly important role in destabi-
18 lizing the layer near and above the cold-point tropopause. Outside of the eye,
19 the upper-tropospheric outflow layer exports high potential temperature (θ)
20 air from the eyewall to large radii in the upper troposphere. This increase in
21 θ forces stabilization below the outflow jet and destabilization above. Vertical
22 wind shear above and below the outflow maximum induces vertical gradi-
23 ents of turbulence, which also modify the vertical stability profile. Mean-
24 while, radiative heating tendencies at the top of the cirrus canopy generally
25 act to destabilize the upper troposphere and stabilize the lower stratosphere.
26 These turbulent and radiative processes combine to play an important role in
27 the development of the strong stable layer immediately above the cold-point
28 tropopause during RI.

29 1. Introduction

30 Using a high-resolution dropsonde dataset collected during the Tropical Cyclone Intensity ex-
31 periment (TCI; Doyle et al. 2017), Duran and Molinari (2018) observed dramatic changes in
32 tropopause structure during the rapid intensification (RI) of Hurricane Patricia (2015). The goal of
33 the present paper is to analyze the processes that might have produced the upper-tropospheric and
34 lower-stratospheric fluctuations observed in Patricia using an idealized axisymmetric simulation.

35 After undergoing a remarkably rapid intensification (RI), Hurricane Patricia (2015) set a new
36 record as the strongest tropical cyclone (TC) ever observed in the Western Hemisphere (Kimber-
37 lain et al. 2016; Rogers et al. 2017). TCI dropsonde observations collected during this RI period
38 revealed dramatic changes in the cold-point tropopause height and upper-level static stability (Du-
39 ran and Molinari 2018). In particular, when Patricia was at tropical storm intensity shortly before
40 RI commenced, a strong inversion layer existed just above the cold-point tropopause. During the
41 first half of the RI period, this inversion layer weakened throughout Patricia’s inner core, with the
42 weakening most pronounced over the developing eye. By the time the storm reached its maximum
43 intensity of 95 m s^{-1} , the inversion layer over the eye had disappeared almost completely, which
44 was accompanied by a greater than 1-km increase in the tropopause height. Meanwhile over the
45 eyewall region, the static stability increased and the tropopause remained near its initial level.

46 Despite the importance of tropopause-layer thermodynamics in theoretical models of hurri-
47 canes (Emanuel and Rotunno 2011; Emanuel 2012), most observational studies of the upper-
48 tropospheric structure of TCs are decades old¹. Recently, however, Komaromi and Doyle (2017)
49 found that stronger TCs tended to have a higher and warmer tropopause over their inner core than
50 weaker TCs. Their results are consistent with the evolution observed over the inner core of Hur-

¹ An in-depth review of these papers can be found in Duran and Molinari (2018).

51 ricane Patricia, in which the tropopause height increased and the tropopause temperature warmed
52 throughout RI (Duran and Molinari 2018).

53 An idealized simulation of a TC analyzed by Ohno and Satoh (2015) suggested that the devel-
54 opment of an upper-level warm core near the 13-km level acted to decrease the static stability near
55 the tropopause within the eye. During the early stage of development in their simulation, large
56 static stability existed above 16 km at all radii (their Fig. 9c). However, after the storm's inten-
57 sification, the static stability within the eye above 16 km was markedly smaller (their Fig. 10c).
58 Although the mechanisms that might drive this static stability evolution have not been examined
59 explicitly, it might be related to the development of an upper-tropospheric warm core within the
60 eye. Stern and Zhang (2013) described the development of the TC warm core using a potential
61 temperature (θ) budget analysis. Although the warm anomaly in their simulation maximized in the
62 mid-levels, they also note that a secondary warming maximum also existed in the 12-14-km layer.
63 They found that radial and vertical advection both played important roles in this warm core devel-
64 opment throughout RI, and subgrid-scale diffusion became particularly important during the later
65 stage of RI. The warming of the upper troposphere by these advective and diffusive processes
66 could contribute to a decrease in static stability near the tropopause within the eye by decreasing
67 the vertical θ gradient.

68 Outside of the eye, in the presence of cirrus clouds, vertical gradients of radiative heating also
69 can modify the tropopause-layer static stability. Bu et al. (2014) note the existence of a shallow
70 region of diurnal-mean net radiative cooling at the top of the TC cirrus canopy (see their Figs. 5,
71 11). This shallow region of cooling could act to destabilize the layer just below the top of the cirrus
72 canopy and stabilize the layer immediately above. If the top of the cirrus canopy lies close to the
73 tropopause, these radiative processes could contribute to a stabilization of the lower stratosphere,
74 as was observed in Hurricane Patricia.

75 To our knowledge, the only paper that has examined explicitly the static stability evolution
76 in a modeled TC is Kepert et al. (2016), but their analysis was limited to the boundary layer.
77 The analysis herein is based upon that of Stern and Zhang (2013), except using a static stability
78 budget similar to that of Kepert et al. (2016), with a focus on the upper-tropospheric and lower-
79 stratospheric evolution during RI.

80 **2. Model Setup**

81 The numerical simulations were performed using version 19.4 of Cloud Model 1 (CM1) de-
82 scribed in Bryan and Rotunno (2009). The equations of motion were integrated on a 3000-km-
83 wide, 30-km-deep axisymmetric grid with 1-km horizontal and 250-m vertical grid spacing. The
84 computations were performed on an f -plane at 15°N latitude, over a sea surface with constant
85 temperature of 30.5°C, which matches that observed near Hurricane Patricia (2015; Kimberlain
86 et al. 2016). Horizontal turbulence was parameterized using the Smagorinsky scheme described
87 in Bryan and Rotunno (2009, pg. 1773), with a prescribed mixing length that varied linearly from
88 100 m at a surface pressure of 1015 hPa to 1000 m at a surface pressure of 900 hPa. Vertical
89 turbulence was parameterized using the formulation of Markowski and Bryan (2016, their Eq.
90 6), using an asymptotic vertical mixing length of 100 m. A Rayleigh damping layer was applied
91 outside of the 2900-km radius and above the 25-km level to prevent spurious gravity wave reflec-
92 tion at the model boundaries. Microphysical processes were parameterized using the Thompson
93 et al. (2004) scheme, and radiative heating tendencies were computed every two minutes using the
94 Rapid Radiative Transfer Model for GCMs (RRTMG) longwave and shortwave schemes (Iacono
95 et al. 2008). The initial temperature and humidity field was horizontally homogeneous and deter-
96 mined by averaging all Climate Forecast System Reanalysis (CFSR) grid points within 100 km of
97 Patricia’s center of circulation at 18 UTC 21 October 2015. The vortex described in Rotunno and

98 Emanuel (1987, their Eq. 37) was used to initialize the wind field, setting all parameters equal to
 99 the values used therein.

100 Although hurricanes simulated in an axisymmetric framework tend to be more intense than
 101 those observed in nature, the intensity evolution of this simulation matches reasonably well with
 102 that observed in Hurricane Patricia. After an initial spin-up period of about 20 hours, the modeled
 103 storm (Fig. 1, blue lines) began an RI period that lasted approximately 18 hours. After this RI, the
 104 storm continued to intensify more slowly until the maximum 10-m wind speed reached 89 m s^{-1}
 105 and the sea-level pressure reached its minimum of 846 hPa 81 hours into the simulation. Hurricane
 106 Patricia (red stars) exhibited a similar intensity evolution prior to its landfall, with an RI period
 107 leading to a maximum 10-m wind speed of 95 m s^{-1} and a minimum sea-level pressure of 872 hPa.

108 3. Budget Computation

109 The static stability can be expressed as the squared Brunt-Väisälä frequency:

$$N_m^2 = \frac{g}{T} \left(\frac{\partial T}{\partial z} + \Gamma_m \right) \left(1 + \frac{T}{R_d/R_v + q_s} \frac{\partial q_s}{\partial T} \right) - \frac{g}{1 + q_t} \frac{\partial q_t}{\partial z}, \quad (1)$$

110 where g is gravitational acceleration, T is temperature, R_d and R_v are the gas constants of dry air
 111 and water vapor, respectively, q_s is the saturation mixing ratio, q_t is the total condensate mixing
 112 ratio, and Γ_m is the moist-adiabatic lapse rate:

$$\Gamma_m = g(1 + q_t) \left(\frac{1 + L_v q_s / R_d T}{c_{pm} + L_v \partial q_s / \partial T} \right), \quad (2)$$

113 where L_v is the latent heat of vaporization and c_{pm} is the specific heat of moist air at constant
 114 pressure. In the tropopause layer, q_s , $\partial q_s / \partial T$, and $\partial q_t / \partial z$ approach zero. In this limiting case,
 115 Eq. 1 reduces to:

$$N^2 = \frac{g}{\theta} \frac{\partial \theta}{\partial z}, \quad (3)$$

116 where θ is the potential temperature.

117 To compute N^2 , CM1 uses Eq. 1 in saturated environments and Eq. 3 in sub-saturated envi-
 118 ronments. For simplicity, however, only Eq. 3 will be employed for the budget computations
 119 throughout the entire domain².

120 Taking the time derivative of Eq. 3 yields the static stability tendency:

$$\frac{\partial N^2}{\partial t} = \frac{g}{\theta} \frac{\partial}{\partial z} \frac{\partial \theta}{\partial t} - \frac{g}{\theta^2} \frac{\partial \theta}{\partial z} \frac{\partial \theta}{\partial t}, \quad (4)$$

121 where the potential temperature tendency, $\partial \theta / \partial t$, can be written, following Bryan (cited 2018):

$$\frac{\partial \theta}{\partial t} = -u \frac{\partial \theta}{\partial r} - w \frac{\partial \theta}{\partial z} + HTURB + VTURB + MP + RAD + DISS \quad (5)$$

122 Each term on the right-hand side of Eq. 5 represents a θ budget variable, each of which is output
 123 directly by the model every minute.

124 The first term on the right-hand side of Eq. 4 is larger than the second term throughout most of
 125 the tropopause layer (not shown). Consequently, the contribution of each of the terms in Eq. 5 to
 126 the N^2 tendency can be interpreted in light of a vertical gradient of each term.

127 Taking the vertical gradient of the first two terms on the right-hand side of Eq. 5 yields the time
 128 tendency of the vertical θ gradient due to horizontal and vertical advection³:

$$\left(\frac{\partial}{\partial t} \frac{\partial \theta}{\partial z} \right)_{adv} = -u \frac{\partial}{\partial r} \frac{\partial \theta}{\partial z} - w \frac{\partial}{\partial z} \frac{\partial \theta}{\partial z} - \frac{\partial u}{\partial z} \frac{\partial \theta}{\partial r} - \frac{\partial w}{\partial z} \frac{\partial \theta}{\partial z}. \quad (6)$$

129 The first two terms on the right-hand side of Eq. 6 represent advection of static stability by the
 130 radial and vertical wind, respectively. These terms act to rearrange the static stability field, but
 131 cannot strengthen or weaken static stability maxima or minima. The third and fourth terms on
 132 the right-hand side of Eq. 6 represent, respectively, the tilting of isentropes in the presence of
 133 vertical wind shear, and the stretching or squashing of isentropes by vertical gradients of vertical

²The validity of this approximation will be substantiated later in this section.

³These terms include the tendencies due to implicit diffusion in the fifth-order finite differencing scheme, which are separated from the advection terms in the CM1 version 19.4 budget output.

134 velocity. Since these terms involve velocity gradients, they can act to strengthen or weaken static
 135 stability maxima or minima through differential advection. Unless otherwise stated, any reference
 136 to "advection" in this paper indicates the sum of all of the terms in Eq. 6.

137 Returning to Eq. 5, HTURB and VTURB are the θ tendencies from the horizontal and vertical
 138 turbulence parameterizations, MP is the tendency from the microphysics scheme, RAD is the
 139 tendency from the radiation scheme, and DISS is the tendency due to turbulent dissipation. This
 140 equation neglects Rayleigh damping, since the entire analysis domain lies outside of the regions
 141 where damping is applied. Each term in Eq. 5 is substituted for $\partial\theta/\partial t$ in Eq. 4, yielding the
 142 contribution of each budget term to the static stability tendency. These terms are summed, yielding
 143 an instantaneous "budget change" in N^2 every minute. The budget changes are then averaged over
 144 24-hour periods and compared to the total model change in N^2 over that same time period, i.e.:

$$\Delta N_{budget}^2 = \frac{1}{\delta t} \sum_{t=t_0}^{t_0+\delta t} \frac{\partial N^2}{\partial t} \Big|_t \quad (7)$$

$$\Delta N_{model}^2 = N_{t_0+\delta t}^2 - N_{t_0}^2 \quad (8)$$

$$Residual = \Delta N_{model}^2 - \Delta N_{budget}^2 \quad (9)$$

147 where t_0 is an initial time and δt is 24 hours.

148 Eqs. 7-9 are plotted for three consecutive 24-hour periods in Fig. 2. For this and all subsequent
 149 radial-vertical cross sections, a 1-2-1 smoother is applied once in the radial direction to eliminate
 150 $2\Delta r$ noise that appears in some of the raw model output and calculated fields. The left column
 151 of Fig. 2 depicts the model changes computed using Eq. 8, together with Eq. 1 in saturated envi-
 152 ronments and Eq. 3 in subsaturated environments. The center column depicts the budget changes
 153 computed using Eq. 7 together with Eq. 3 throughout the entire domain. Thus, the left column
 154 includes the effect of moisture in the N^2 computations, whereas the center column neglects mois-
 155 ture. The right column depicts the residuals, computed using Eq. 9 (i.e. the left column minus

156 the center column.) In every 24-hour period, the budget changes are nearly identical to the model
157 changes, which is reflected in the near-zero residuals in the right column. This indicates that the
158 budget accurately represents the model variability, which implies that the neglect of moisture in
159 the budget computation introduces negligible error within the analysis domain⁴.

160 In the tropopause layer, some of the budget terms are small enough to be ignored. To determine
161 which of the budget terms are most important, a time series of the contribution of each of the
162 budget terms in Eq. 5 to the tropopause-layer static stability tendency is plotted in Fig. 3. For this
163 figure, each of the budget terms is computed using the method described in Section 3, except with
164 1-hour averaging intervals instead of 24-hour intervals. The absolute values of these tendencies
165 are then averaged over the radius-height domain of the plots shown in Fig. 2 and plotted as a time
166 series⁵. Advection (Fig. 3, red line) plays an important role in the mean tropopause-layer static
167 stability tendency at all times, and vertical turbulence (Fig. 3, blue line) and radiation (Fig. 3, dark
168 green line) also contribute significantly. The remaining three processes - horizontal turbulence,
169 microphysics, and dissipative heating - are negligible everywhere outside of the eyewall, and do
170 not play important roles in the mesoscale tropopause variability.

171 The preceding analysis indicates that, at all times, three budget terms dominate the tropopause-
172 layer static stability tendency: advection, vertical turbulence, and radiation. Variations in the
173 magnitude and spatial structure of these terms drive the static stability changes depicted in Fig. 2;
174 subsequent sections will focus on these variations and what causes them.

⁴This is not the case in the lower- and mid-troposphere, where the residual actually exceeds the budget tendencies in many places, likely due to the neglect of moisture; thus we limit this analysis to the upper troposphere and lower stratosphere.

⁵It will be seen in subsequent figures that each of the terms contributes both positively and negatively to the N^2 tendency within the analysis domain. Thus, taking an average over the domain tends to wash out the positive and negative contributions. To circumvent this problem, the absolute value of each of the terms is averaged.

4. Results

a. Static stability evolution

The average N^2 over the first day of the simulation (Fig. 4a) indicates the presence of a weak N^2 maximum just above the cold-point tropopause. Over the subsequent 24 hours, during the RI period, the N^2 within and above this layer decreased within the 25-km radius (Fig. 4b). This decreasing N^2 corresponded to an increase in the tropopause height within the developing eye, maximized at the storm center. Outside of the eye, meanwhile, the tropopause height decreased over the eyewall region (25-60-km radius) and increased only slightly outside of the 60-km radius. In this outer region, the N^2 maximum just above the tropopause strengthened during RI. These trends continued as the storm's intensity leveled off in the 48-72-hour period (Fig. 4c). The tropopause height increased to nearly 21 km at the storm center and sloped sharply downward to 16.3 km on the inner edge of the eyewall, near the 30 km radius. Static stability outside of the eye, meanwhile, continued to increase just above the cold-point tropopause. This N^2 evolution closely follows that observed in Hurricane Patricia (2015; Duran and Molinari 2018, see their Fig. 4). The mechanisms that led to these N^2 changes will be investigated in the subsequent sections.

b. Static stability budget analysis

(i) 0-24 hours

The initial spin-up period was characterized by a steady increase of the maximum wind speed from 11 m s⁻¹ to 22 m s⁻¹ (Fig. 1a, blue line), an intensification rate that closely matched that of TC Patricia (Fig. 1a, red stars). The weakening of the lower-stratospheric static stability maximum during this period is reflected in the total N^2 budget change over this time (Fig. 5a). The layer just above the cold-point tropopause was characterized by decreasing N^2 (purple shading), maximizing

197 at the storm center. At and immediately below the tropopause, meanwhile, N^2 increased during
 198 this time period (green shading). Although these tendencies extended out to the 200-km radius,
 199 they were particularly pronounced at innermost radii. A comparison of the contributions of advec-
 200 tion (Fig. 5b), vertical turbulence (Fig. 5c), and radiation (Fig. 5d) reveals that advection was the
 201 primary driver of the N^2 tendency during this period, acting to stabilize near and just below the
 202 tropopause and destabilize above. Although vertical turbulence acted in opposition to advection
 203 (i.e. it acted to stabilize regions that advection acted to destabilize), the magnitude of the advec-
 204 tive tendencies was larger, particularly at the innermost radii. The sum of advection and vertical
 205 turbulence (Fig. 5e) almost exactly replicated the static stability tendencies above the tropopause.
 206 Radiative tendencies, meanwhile, (Fig. 5d) acted to destabilize the layer below about 16 km and
 207 stabilize the layer between 16 and 17 km. The sum of advection, vertical turbulence, and radiation
 208 (Fig. 5f) reproduced the total change in N^2 almost exactly.

209 (ii) 24-48 hours

210 During the RI period, the maximum wind speed increased from 22 m s^{-1} to 80 m s^{-1} (Fig. 1a).
 211 Over this time, N^2 within the eye generally decreased above 16 km and increased below (Fig. 6a),
 212 with the destabilization above 16 km maximizing near the level of the mean cold-point tropopause.
 213 These tendencies at the innermost radii were driven almost entirely by advection (Fig. 6b). Vertical
 214 turbulence (Fig. 6c) and radiation (Fig. 6d) contributed negligibly to the static stability tendencies
 215 in this region.

216 Outside of the eye, the N^2 evolution exhibited alternating layers of positive and negative tenden-
 217 cies. Near and above 18 km existed an upward-sloping region of decreasing N^2 that extended out
 218 to the 180-km radius. In this region, neither vertical turbulence nor radiation exhibited negative N^2
 219 tendencies; advection was the only forcing for this destabilization. Immediately below this layer,

220 just above the cold-point tropopause, was a region of increasing N^2 that sloped upward from 17
 221 km near the 30-km radius to just below 18 km outside of the 100-km radius. Advection and verti-
 222 cal turbulence both contributed to this positive N^2 tendency, with advection playing an important
 223 role below about 17.5 km and and turbulence playing an important role above. The sum of advec-
 224 tion and turbulence (Fig. 6e) reveals two separate regions of increasing N^2 in the 17-18-km layer
 225 rather than one contiguous region. The addition of radiation to these two terms, however, (Fig. 6f)
 226 provides the link between these two regions, indicating that radiation also plays a role in strength-
 227 ening the stable layer just above the tropopause. In the 16-17-km layer, just below the cold-point
 228 tropopause, a horizontally-extensive layer of destabilization also was forced by a combination of
 229 advection, vertical turbulence, and radiation. The sum of advection and vertical turbulence ac-
 230 counts for only a portion of the decreasing N^2 in this layer, and actually indicates forcing for
 231 stabilization near the 50-km radius and outside of the 130-km radius. Radiative tendencies over-
 232 come this forcing for stabilization in both of these regions to produce the radially-extensive region
 233 of destabilization observed just below the tropopause.

234 The sum of advection, vertical turbulence, and radiation (Fig. 6f) once again closely follows
 235 the observed N^2 variability, except in the eyewall region, where the neglect of latent heating and
 236 horizontal turbulence introduces some differences.

237 *(iii) 48-72 hours*

238 After the storm's maximum wind speed leveled off near 80 m s^{-1} (Fig. 1a), the magnitude of
 239 the static stability tendencies within the eye decreased to near zero (Fig. 7a). Outside of the eye,
 240 however, N^2 continued to decrease in the layer immediately surrounding the tropopause and in-
 241 crease just above. The sum of advection and vertical turbulence (Fig. 7e) indicates that these two
 242 processes account for most of the destabilization near the tropopause and some of the stabilization

243 near the 18-km altitude. Below the tropopause, however, these two terms provided strong forcing
 244 for stabilization that was not observed in the budget change (Fig. 7a). Radiation (Fig. 7d), which
 245 generally forced stabilization above 17 km and destabilization below, balanced out this forcing
 246 for stabilization in the upper troposphere. In the eyewall region (30-80-km radius), advection and
 247 vertical turbulence combined to force destabilization in the 17-18-km layer (Fig. 7e), which was
 248 not observed in the budget change (Fig. 7a). Radiation provided strong forcing for stabilization,
 249 which outweighed this effect and produced net stabilization in a portion of this region. Outside of
 250 the 80-km radius, both advection (Fig. 7b) and vertical turbulence (Fig. 7c) provided forcing for
 251 stabilization near and just above the 18-km level. The sum of the two terms (Fig. 7e) indicates
 252 increasing N^2 near the 18-km level everywhere outside of the 80-km radius, but this stabilization
 253 is slightly weaker in the 90-120-km radial band than the observed value. The addition of radiation
 254 (Fig. 7f) provided the extra forcing for stabilization required to account for the observed increase
 255 in N^2 . Outside of the 120-km radius, the region of radiative forcing for stabilization sloped down-
 256 ward, and the increase in N^2 observed near 18 km can be explained entirely by a combination of
 257 advection and vertical turbulence.

258 **5. Discussion**

259 *a. The role of advection*

260 Advection played an important role in the tropopause-layer N^2 evolution at all stages of intensifi-
 261 cation, but for brevity, this section will focus only on the RI (24-48-hour) period. To investigate the
 262 advective processes more closely, the individual contributions of horizontal and vertical advection
 263 during the RI period are shown in Fig. 8, along with the corresponding time-mean radial and verti-
 264 cal velocities and θ . The N^2 tendencies due to the two advective components (Fig. 8a,b) exhibited

265 strong cancellation, consistent with flow that was nearly isentropic. There existed, however, a
266 large region near the tropopause in which the total advective tendency was nonzero (Fig. 6b).
267 These nonzero tendencies were related to the development of the TC's secondary circulation as
268 the storm intensified.

269 During the RI period, strong radial and vertical circulations developed near the tropopause
270 (Fig. 8c,d), which forced high-magnitude N^2 tendencies due to advection (Fig. 8a,b). A layer
271 of strong outflow formed at and below the tropopause during this period, with the outflow maxi-
272 mum (dashed cyan line) curving from the 14-km level at the 50-km radius to just below the 16-km
273 level outside of the 80-km radius (Fig. 8c). Notably, the N^2 tendency due to horizontal advection
274 (Fig. 8a) tended to switch signs at this line, with stabilization below the outflow maximum and
275 destabilization above. This is consistent with the outflow layer carrying air with increasingly large
276 θ from the eyewall to large radii as the storm intensified. This increase in θ maximized near the
277 outflow maximum, which acted to decrease $\partial\theta/\partial z$ above the outflow maximum and increase it be-
278 low. This mechanism is the same as that discussed in Trier and Sharman (2009), in which vertical
279 wind shear in the outflow layer of a mesoscale convective system modified the upper-tropospheric
280 static stability through differential advection of isentropes.

281 Meanwhile in the lower stratosphere, a thin layer of 2-4 m s⁻¹ inflow developed a few hundred
282 meters above the tropopause, similar to that which was observed in Hurricane Patricia (2015;
283 Duran and Molinari 2018) and in previous modeling studies (e.g. Ohno and Satoh 2015; Kieu et al.
284 2016). Since the isentropes in this layer sloped slightly upward with radius (i.e. $\partial\theta/\partial r < 0$), this
285 inflow acted to import lower θ air from outer radii to inner radii. Since the negative θ tendencies
286 maximized at the level of maximum inflow, the layer below the inflow maximum destabilized and
287 the layer above stabilized (Fig. 8a).

Curiously, horizontal advection contributed to the N^2 tendency everywhere within the eye, even though the mean radial velocity there was near zero. Close examination of the model output revealed that these tendencies were forced by advective processes associated with inward-propagating waves. Although the radial velocity perturbations induced by these waves averaged out to zero, the advective tendencies forced by the radial velocity perturbations did not. Additionally, when these waves reached $r=0$, a dipole of vertical velocity resulted, with ascent above and descent below. For reasons that remain unclear, the regions of ascent were more persistent than the regions of descent, which resulted in the mean ascent observed near $r=0$ above 17 km in Fig. 8d.

Vertical advection also played an important role in the tropopause-layer static stability evolution. Within the eye, subsidence dominated below 17 km, while mean ascent existed near the storm center above 17 km. Although the magnitude of the subsidence was larger at lower altitudes, $\partial\theta/\partial z$ was smaller there. Because $\partial\theta/\partial z$ was smaller, the subsidence at lower levels could not accomplish as much warming as the subsidence at higher levels in the eye, consistent with the results of Stern and Zhang (2013). As a result, vertical advection within the eye stabilized the layer below 16 km during RI.

Outside of the 27-km radius, ascent dominated the troposphere, while a 1-1.5-km-deep layer of descent existed immediately above the tropopause. These regions of ascent and descent converged just above the tropopause; this convergence acted to compact the isentropes in this layer and increase the static stability. Above the lower-stratospheric subsidence maximum, meanwhile, vertical advection decreased N^2 . Below the tropopause, differential vertical advection increased N^2 within the eyewall region and also at larger radii above the vertical velocity maximum at larger radii. Outside of the eyewall and below the vertical velocity maximum, meanwhile, differential vertical advection acted to decrease N^2 .

311 Comparing the N^2 tendencies forced by horizontal (Fig. 8a) and vertical (Fig. 8b) advection
312 to the total advective tendency seen in Fig. 6b reveals that horizontal advective tendencies domi-
313 nated the troposphere, while vertical advective tendencies dominated the layer near and above the
314 tropopause. Thus, tilting of isentropes in the vicinity of the upper-tropospheric outflow maximum
315 appears to be the most important advective process governing the N^2 tendency in the troposphere,
316 whereas convergence of vertical velocity appears to be the most important advective process near
317 the tropopause.

318 *b. The role of radiation*

319 During the initial spin-up period (0-24 hours; Fig. 9a), convection was not deep enough to
320 deposit large quantities of ice near the tropopause and create a persistent cirrus canopy. Due to the
321 lack of ice particles, the radiative heating tendencies during this period (Fig. 9b) were relatively
322 small and confined to the region above a few particularly strong, although transient, convective
323 towers. During RI (24-48 hours), the eyewall updraft strengthened and a radially-extensive cirrus
324 canopy developed near the tropopause (Fig. 9c). The enhanced vertical gradient of ice mixing ratio
325 at the top of the cirrus canopy induced strong diurnal-mean radiative cooling near the tropopause
326 (Fig. 9d). This cooling exceeded 0.6 K h^{-1} (14.4 K day^{-1}) in some places and sloped downward
327 from the lower stratosphere into the upper troposphere, following the top of the cirrus canopy. A
328 small radiative warming maximum also appeared outside of the 140-km radius below this region
329 of cooling. These results broadly agree with those of Bu et al. (2014; see their Fig. 11a), whose
330 CM1 simulations produced a 0.3 K h^{-1} diurnally-averaged radiative cooling at the top of the cirrus
331 canopy and radiative warming within the cloud that maximized near the 200-km radius. This broad
332 region of radiative cooling acted to destabilize the layer below the cooling maximum and stabilize
333 the layer above, which can be seen in Fig. 6d. The small area of net radiative heating outside of

the 140-km radius enhanced the destabilization above 16 km in this region and produced a thin layer of stabilization in the 15-16-km layer.

After the TC's RI period completed (48-72 hours), strong radiative cooling remained near the tropopause at inner radii (Fig. 9f), sloping downward with the top of the cirrus canopy to below the tropopause at outer radii. Cooling rates exceeded 1 K h^{-1} (24 K day^{-1}) just above the tropopause between the 30- and 70-km radii. This value is more than three times the maximum cooling rate of 0.3 K h^{-1} observed by Bu et al. (2014), a difference that is a consequence of their larger vertical grid spacing compared to that used here, along with a contribution from differing radiation schemes. To compare our results to theirs, we ran a simulation identical to that described in Section 2, except using the NASA-Goddard radiation scheme and 625-m vertical grid spacing, to match those of Bu et al. (2014). This simulation produced a maximum 24-hour-average radiative cooling rate of 0.3 K h^{-1} , which agrees with that shown in Bu et al. (2014). Another simulation using 625-m vertical grid spacing and RRTMG radiation produced 24-hour-average cooling rates of up to 0.6 K h^{-1} . This suggests that vertical grid spacing smaller than 625 m is necessary to resolve properly the radiative cooling at the top of the cirrus canopy, and that the results can be quite sensitive to the radiation scheme used.

Meanwhile below the tropopause, time-mean radiative warming spread from 30- to 160-km radius within the cirrus canopy. The existence of radiative cooling overlying radiative warming in this region led to radiatively-forced destabilization at and below the tropopause, as was observed in Fig. 7d. Beneath the warming layer existed a region of forcing for stabilization, while a much stronger region of forcing for stabilization existed in the lower stratosphere, above the cooling maximum.

The results herein suggest that, after the cirrus canopy developed, radiative heating tendencies considerably destabilized the upper troposphere and stabilized the lower stratosphere.

358 *c. The role of turbulent mixing*

359 Fig. 10 depicts the effect of turbulent mixing on the vertical θ profile of an initially stably-
360 stratified layer. At the initial time in this schematic, θ is assumed to increase with height at a
361 constant rate (Fig. 10, left panel). The imposition of turbulence (blue hatching) adjusts the θ
362 profile within the mixed layer toward a constant value equal to the mean value of that layer in
363 the initial state (Fig. 10, right panel). Just above and just below the mixed layer, however, the θ
364 profile remains undisturbed. Consequently, although turbulent mixing acts to decrease $\partial\theta/\partial z$ in
365 the layer in which it is occurring, it actually increases $\partial\theta/\partial z$ just below and just above the layer.
366 Vertical gradients of turbulent mixing like those depicted here are quite important, particularly on
367 the flanks of the upper-tropospheric outflow jet.

368 Two distinct maxima of vertical eddy diffusivity developed in the tropopause layer as the storm
369 intensified (Fig. 11). Comparison of these turbulent regions to the N^2 tendencies in Figs. 6c and
370 7c reveals that the layers in which vertical eddy diffusivity maximized corresponded to layers of
371 destabilization due to vertical turbulence. Just outside of these layers, however, vertical turbulence
372 acted to increase N^2 . The large vertical gradient of vertical eddy diffusivity near the tropopause
373 played an important role in developing the lower-stratospheric stable layer during RI. These results
374 support the hypothesized role of turbulence in setting the outflow-layer θ stratification in Rotunno
375 and Emanuel (1987).

376 **6. Conclusions**

377 The simulated N^2 evolution shown herein closely matched that observed during the RI of Hur-
378 ricane Patricia (2015). Three N^2 budget terms dominated in the upper troposphere and lower
379 stratosphere: advection, radiation, and vertical turbulence. Advection dominated within the eye,
380 where it provided forcing for destabilization. Radiation and vertical turbulence played particularly

important roles in developing the strong N^2 maximum just above the cold-point tropopause during RI.

To put the N^2 variability observed near the tropopause into context, Fig. 12 depicts the model change in N^2 over the RI period (hours 24-48) from 0 to 21 km altitude, along with the vertical eddy diffusivity and the radiative heating rate. The largest changes in N^2 occurred in a relatively shallow layer immediately surrounding the tropopause (Fig. 12a). This shallow layer also contained the largest diurnally-averaged radiative heating tendencies found anywhere in the domain (Fig. 12c). Values of vertical eddy diffusivity larger than any found outside of the boundary layer also resided in the upper troposphere (Fig. 12b). The results herein suggest that this turbulence not only develops as a response to the presence of small static stability and large vertical wind shear, as discussed by Molinari et al. (2014) and Duran and Molinari (2016), but also can actively increase the static stability in highly localized regions just above and below the mixed layers.

Since two of the most important processes contributing to the N^2 variability are parameterized, and one (radiation) closely depends on yet another parameterized process (microphysics), the tropopause-layer N^2 variability could be quite sensitive to the assumptions inherent to the parameterizations used. A better understanding of the microphysical characteristics of the TC cirrus canopy, its interaction with radiation, and outflow-layer turbulence is critical to understanding the tropopause-layer N^2 evolution.

In this paper, all of the variables were averaged over a full diurnal cycle to eliminate the effects of diurnal variability and isolate the overall storm evolution. Diurnal variations in static stability near the tropopause are potentially of interest with respect to the tropical cyclone diurnal cycle, and will be the subject of future work.

403 *Acknowledgments.* We are indebted to George Bryan for his continued development and support
404 of Cloud Model 1. We also thank Jeffrey Kepert, Robert Fovell, and Erika Navarro for helpful
405 conversations related to this work. This research was supported by NSF grant AGS-1636799 and
406 Office of Naval Research Grant N000141712110 as a part of the TCI Departmental Research
407 Initiative.

408 **References**

- 409 Bryan, G. H., cited 2018: The governing equations for CM1. [Available online at http://www2.mmm.ucar.edu/people/bryan/cm1/cm1_equations.pdf].
- 410
- 411 Bryan, G. H., and R. Rotunno, 2009: The maximum intensity of tropical cyclones in axisymmetric
412 numerical model simulations. *Mon. Wea. Rev.*, **137**, 1770–1789.
- 413 Bu, Y. P., R. G. Fovell, and K. L. Corbosiero, 2014: Influence of cloud-radiative forcing on tropical
414 cyclone structure. *J. Atmos. Sci.*, **71**, 1644–1622.
- 415 Doyle, J. D., and Coauthors, 2017: A view of tropical cyclones from above: The Tropical Cyclone
416 Intensity (TCI) Experiment. *Bull. Amer. Meteor. Soc.*, **98**, 2113–2134.
- 417 Duran, P., and J. Molinari, 2016: Upper-tropospheric low Richardson number in tropical cyclones:
418 Sensitivity to cyclone intensity and the diurnal cycle. *J. Atmos. Sci.*, **73**, 545–554.
- 419 Duran, P., and J. Molinari, 2018: Dramatic inner-core tropopause variability during the rapid
420 intensification of Hurricane Patricia (2015). *Mon. Wea. Rev.*, **146**, 119–134.
- 421 Emanuel, K., 2012: Self-stratification of tropical cyclone outflow. Part II: Implications for storm
422 intensification. *J. Atmos. Sci.*, **69**, 988–996.

423 Emanuel, K., and R. Rotunno, 2011: Self-stratification of tropical cyclone outflow. Part I: Impli-
 424 cations for storm structure. *J. Atmos. Sci.*, **68**, 2236–2249.

425 Iacono, M. J., J. S. Delamere, E. J. Mlawer, M. W. Shephard, S. A. Clough, and W. D. Collins,
 426 2008: Radiative forcing by long-lived greenhouse gases: Calculations with the AER radiative
 427 transfer models. *J. Geophys. Res.*, **113** (D13103).

428 Kepert, J. D., J. Schwendike, and H. Ramsay, 2016: Why is the tropical cyclone boundary layer
 429 not "well mixed"? *J. Atmos. Sci.*, **73**, 957–973.

430 Kieu, C., V. Tallapragada, D.-L. Zhang, and Z. Moon, 2016: On the development of double warm-
 431 core structures in intense tropical cyclones. *J. Atmos. Sci.*, **73**, 4487–4506.

432 Kimberlain, T. B., E. S. Blake, and J. P. Cangialosi, 2016: Tropical cyclone report: Hurricane
 433 Patricia. National Hurricane Center. [Available online at www.nhc.noaa.gov].

434 Komaromi, W. A., and J. D. Doyle, 2017: Tropical cyclone outflow and warm core structure as
 435 revealed by HS3 dropsonde data. *Mon. Wea. Rev.*, **145**, 1339–1359.

436 Markowski, P. M., and G. H. Bryan, 2016: LES of laminar flow in the PBL: A potential problem
 437 for convective storm simulations. *Mon. Wea. Rev.*, **144**, 1841–1850.

438 Molinari, J., P. Duran, and D. Vollaro, 2014: Low Richardson number in the tropical cyclone
 439 outflow layer. *J. Atmos. Sci.*, **71**, 3164–3179.

440 Ohno, T., and M. Satoh, 2015: On the warm core of a tropical cyclone formed near the tropopause.
 441 *J. Atmos. Sci.*, **72**, 551–571.

442 Rogers, R. F., S. Aberson, M. M. Bell, D. J. Cecil, J. D. Doyle, J. Morgerman, L. K. Shay, and
 443 C. Velden, 2017: Re-writing the tropical record books: The extraordinary intensification of
 444 Hurricane Patricia (2015). *Bull. Amer. Meteor. Soc.*, **98**, 2091–2112.

445 Rotunno, R., and K. A. Emanuel, 1987: An air-sea interaction theory for tropical cyclones. Part II:
446 Evolutionary study using a nonhydrostatic axisymmetric numerical model. *J. Atmos. Sci.*, **44**,
447 542–561.

448 Stern, D. P., and F. Zhang, 2013: How does the eye warm? Part I: A potential temperature budget
449 analysis of an idealized tropical cyclone. *J. Atmos. Sci.*, **70**, 73–89.

450 Thompson, G., R. M. Rasmussen, and K. Manning, 2004: Explicit forecasts of winter precipitation
451 using an improved bulk microphysics scheme. Part I: Description and sensitivity analysis. *Mon.*
452 *Wea. Rev.*, **132**, 519–542.

453 Trier, S. B., and R. D. Sharman, 2009: Convection-permitting simulations of the environment sup-
454 porting widespread turbulence within the upper-level outflow of a mesoscale convective system.
455 *Mon. Wea. Rev.*, **137**, 1972–1990.

456 LIST OF FIGURES

- 457 **Fig. 1.** The maximum 10-m wind speed (top panel; m s^{-1}) and minimum sea-level pressure (bottom
458 panel; hPa) in the simulated storm (blue lines; plotted every minute) and from Hurricane
459 Patricia's best track (red stars; plotted every six hours beginning at the time Patricia attained
460 tropical storm intensity). The rapid weakening during the later stage of Patricia's lifetime
461 was induced by landfall. 26
- 462 **Fig. 2.** Left panels: Twenty-four-hour changes in squared Brunt-Väisälä frequency (N^2 ; 10^{-4} s^{-2})
463 computed using Eq. 8 over (top row) 0-24 hours, (middle row) 24-48 hours, (bottom row)
464 48-72 hours. Middle Panels: The N^2 change over the same time periods computed using Eqs.
465 4-7, Right Panels: The budget residual over the same time periods, computed by subtracting
466 the budget change (middle column) from the model change (left column). Orange lines
467 represent the cold-point tropopause height averaged over the same time periods. 27
- 468 **Fig. 3.** Time series of the contribution of each of the budget terms to the time tendency of the
469 squared Brunt-Väisälä frequency (N^2 ; 10^{-4} s^{-2}). For each budget term, the absolute value
470 of the N^2 tendency is averaged temporally over 1-hour periods (using output every minute),
471 and spatially in a region extending from 0 to 200 km radius and 14 to 21 km altitude. 28
- 472 **Fig. 4.** Twenty-four-hour averages of squared Brunt-Väisälä frequency (N^2 ; 10^{-4} s^{-2}) over (a) 0-24
473 hours, (b) 24-48 hours, (c) 48-72 hours. Orange lines represent the cold-point tropopause
474 height averaged over the same time periods. 29
- 475 **Fig. 5.** (a) Total change in N^2 over the 0-24-hour period ($10^{-4} \text{ s}^{-2} (24 \text{ h})^{-1}$) and the contributions to
476 that change from (b) the sum of horizontal and vertical advection, (c) vertical turbulence, (d)
477 longwave and shortwave radiation, (e) the sum of horizontal advection, vertical advection,

478	and vertical turbulence, and (f) the sum of horizontal advection, vertical advection, vertical	
479	turbulence, and longwave and shortwave radiation. Green shading indicates regions of sta-	
480	bilization and purple shading indicates regions of destabilization. Orange lines represent the	
481	cold-point tropopause height averaged over the 0-24-hour period.	31
482	Fig. 6. As in Fig. 5, but for the 24-48-hour period.	32
483	Fig. 7. As in Fig. 5, but for the 48-72-hour period.	33
484	Fig. 8. The contributions to the change in N^2 over the 24-48-hour period ($10^{-4} \text{ s}^{-2} (24 \text{ h})^{-1}$) by	
485	(a) horizontal advection and (b) vertical advection. (c) The radial velocity (m s^{-1} ; filled con-	
486	tours), potential temperature (K; thick black contours), cold-point tropopause height (orange	
487	line), and level of maximum outflow (dashed cyan line) averaged over the 24-48-hour period.	
488	(d) The vertical velocity (cm s^{-1} ; filled contours), potential temperature (K; thick black con-	
489	tours), and cold-point tropopause height (orange line) averaged over the 24-48-hour period.	
490	34	
491	Fig. 9. Ice mixing ratio (g kg^{-1}) and cold-point tropopause height (orange lines) averaged over (a)	
492	0-24 hours, (c) 24-48 hours, and (e) 48-72 hours. Radiative heating rate (K h^{-1}) and cold-	
493	point tropopause height (orange lines) averaged over (b) 0-24 hours, (d) 24-48 hours, and (f)	
494	48-72 hours.	36
495	Fig. 10. Schematic diagram of the effect of turbulent mixing on the vertical profile of potential tem-	
496	perature (θ). At the initial time (left panel), potential temperature is assumed to increase	
497	with height at a constant rate (thick black line). The imposition of turbulence within a por-	
498	tion of the layer (blue hatching) adjusts the potential temperature profile toward the mean	

499 initial value of that layer. After a period of mixing (right panel) the potential temperature in
 500 the mixed layer does not vary with height, but just above and just below the mixed layer, it
 501 rapidly increases with height. 37

502 **Fig. 11.** Vertical eddy diffusivity ($\text{m}^2 \text{s}^{-2}$; filled contours), cold-point tropopause height (cyan lines),
 503 and radial velocity (m s^{-1} ; thick black lines) averaged over (a) 0-24 hours, (b) 24-48 hours,
 504 and (c) 48-72 hours. 38

505 **Fig. 12.** (Top panel) Change in N^2 over the 24-48-hour period ($10^{-4} \text{s}^{-2} (24 \text{ h})^{-1}$) directly output by
 506 the model for the 0-21-km layer. (Middle panel) Vertical eddy diffusivity ($\text{m}^2 \text{s}^{-2}$) averaged
 507 over the same time period. (Bottom panel) Radiative heating rate (K h^{-1}) averaged over the
 508 same time period. 40

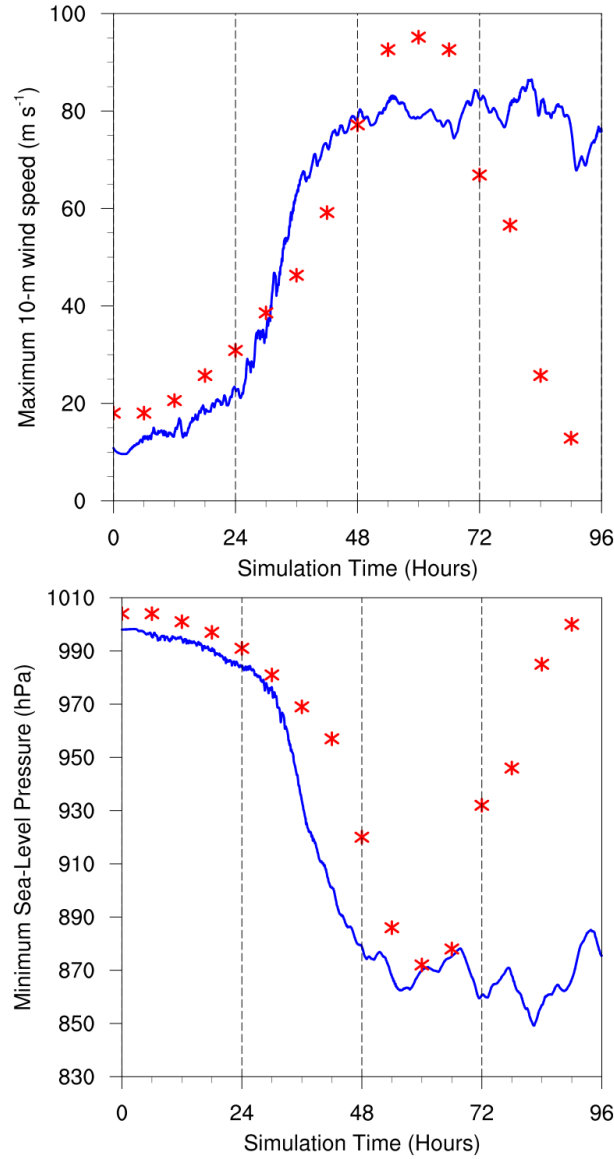


FIG. 1. The maximum 10-m wind speed (top panel; m s^{-1}) and minimum sea-level pressure (bottom panel; hPa) in the simulated storm (blue lines; plotted every minute) and from Hurricane Patricia's best track (red stars; plotted every six hours beginning at the time Patricia attained tropical storm intensity). The rapid weakening during the later stage of Patricia's lifetime was induced by landfall.

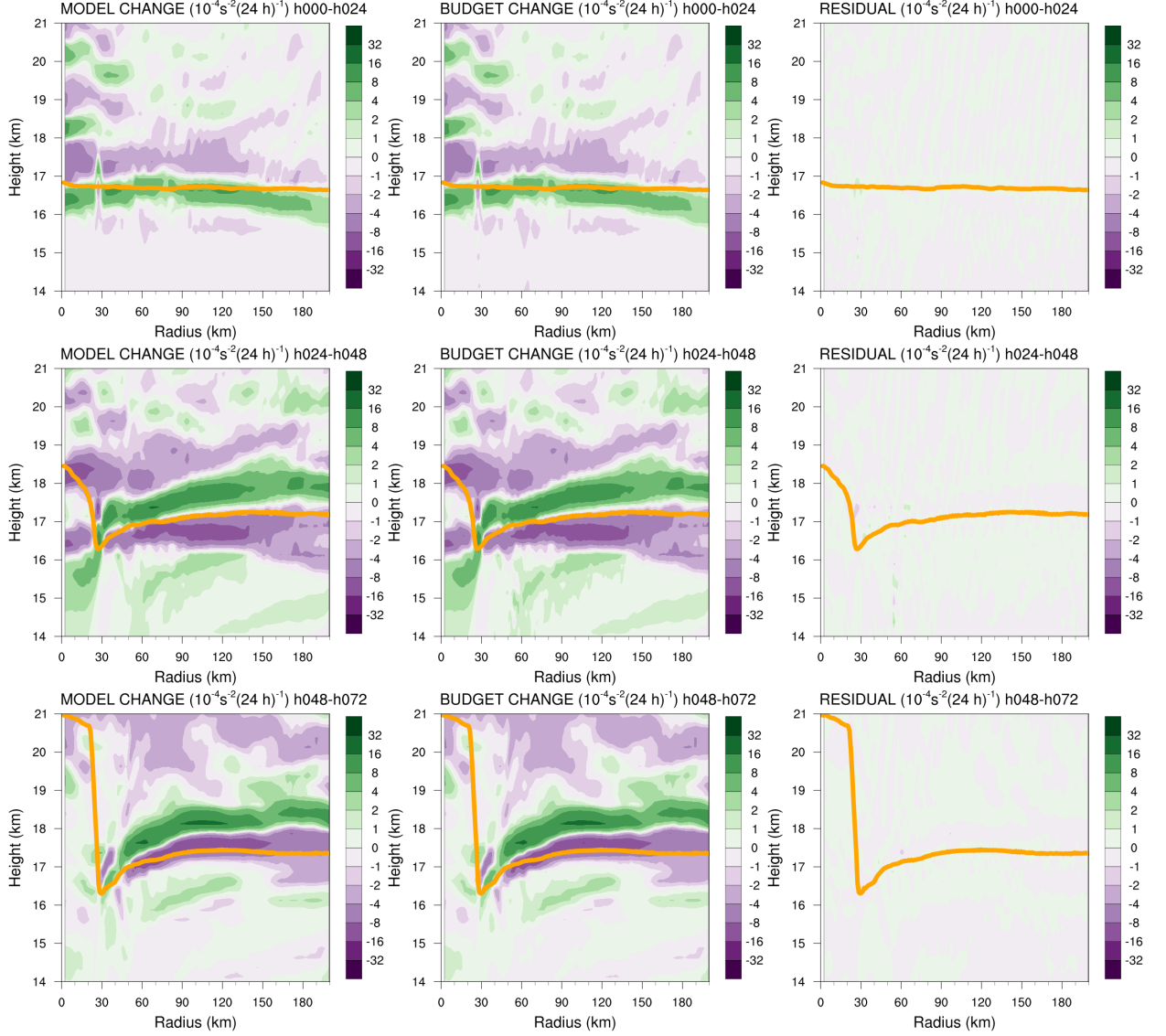


FIG. 2. Left panels: Twenty-four-hour changes in squared Brunt-Väisälä frequency (N^2 ; 10^{-4} s^{-2}) computed using Eq. 8 over (top row) 0-24 hours, (middle row) 24-48 hours, (bottom row) 48-72 hours. Middle Panels: The N^2 change over the same time periods computed using Eqs. 4-7, Right Panels: The budget residual over the same time periods, computed by subtracting the budget change (middle column) from the model change (left column). Orange lines represent the cold-point tropopause height averaged over the same time periods.

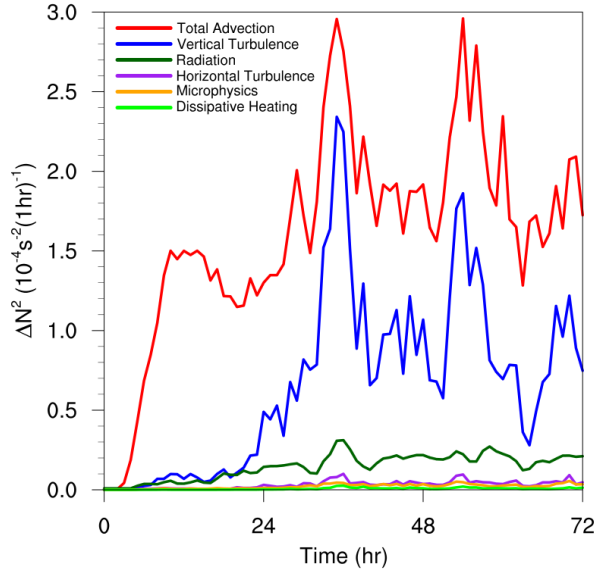


FIG. 3. Time series of the contribution of each of the budget terms to the time tendency of the squared Brunt-Väisälä frequency (N^2 ; 10^{-4} s^{-2}). For each budget term, the absolute value of the N^2 tendency is averaged temporally over 1-hour periods (using output every minute), and spatially in a region extending from 0 to 200 km radius and 14 to 21 km altitude.

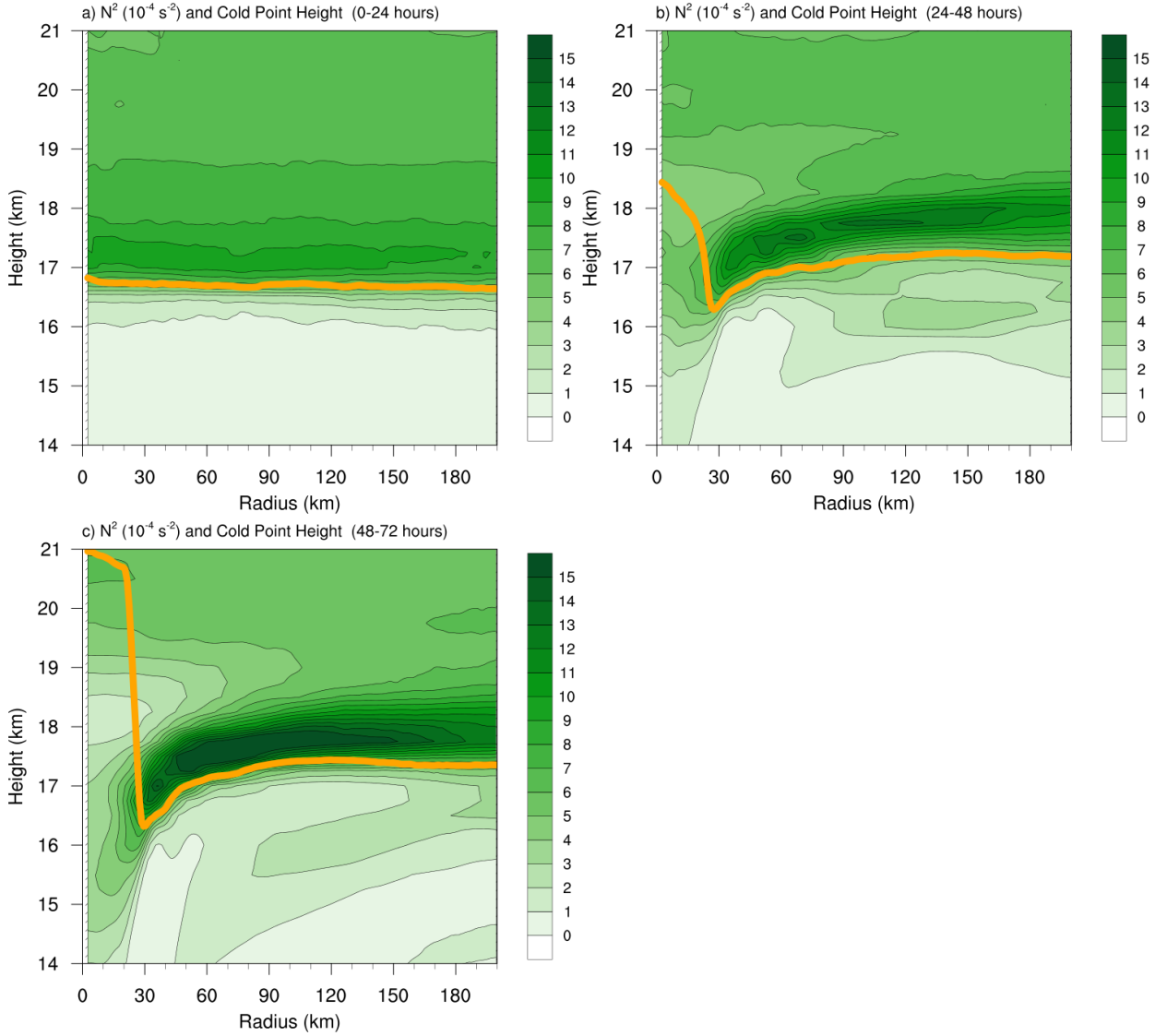
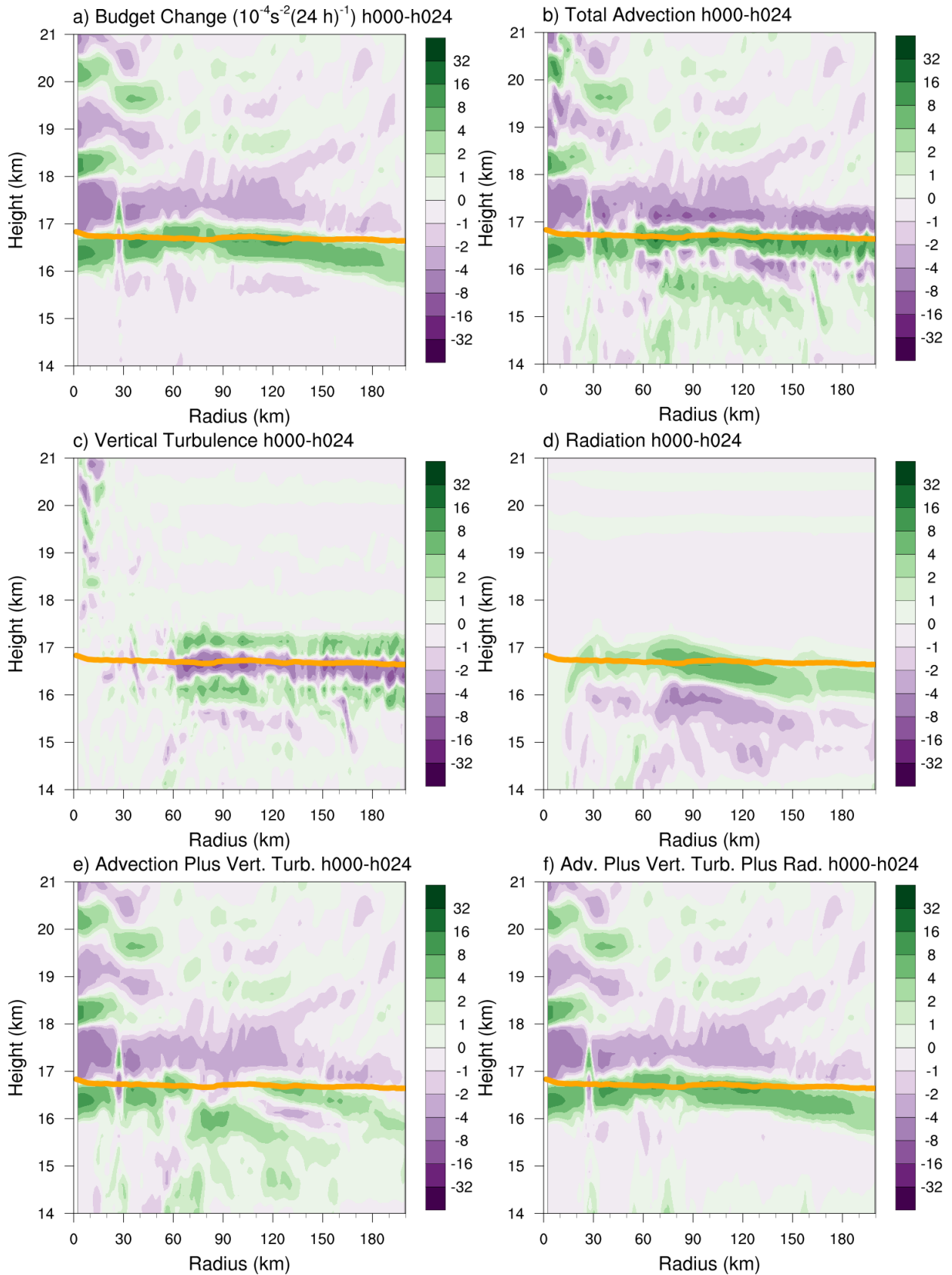


FIG. 4. Twenty-four-hour averages of squared Brunt-Väisälä frequency (N^2 ; 10^{-4} s^{-2}) over (a) 0-24 hours, (b) 24-48 hours, (c) 48-72 hours. Orange lines represent the cold-point tropopause height averaged over the same time periods.



525 FIG. 5. (a) Total change in N^2 over the 0-24-hour period ($10^{-4} \text{ s}^{-2} (24 \text{ h})^{-1}$) and the contributions to that change
 526 from (b) the sum of horizontal and vertical advection, (c) vertical turbulence, (d) longwave and shortwave
 527 radiation, (e) the sum of horizontal advection, vertical advection, and vertical turbulence, and (f) the sum of
 528 horizontal advection, vertical advection, vertical turbulence, and longwave and shortwave radiation. Green
 529 shading indicates regions of stabilization and purple shading indicates regions of destabilization. Orange lines
 530 represent the cold-point tropopause height averaged over the 0-24-hour period.

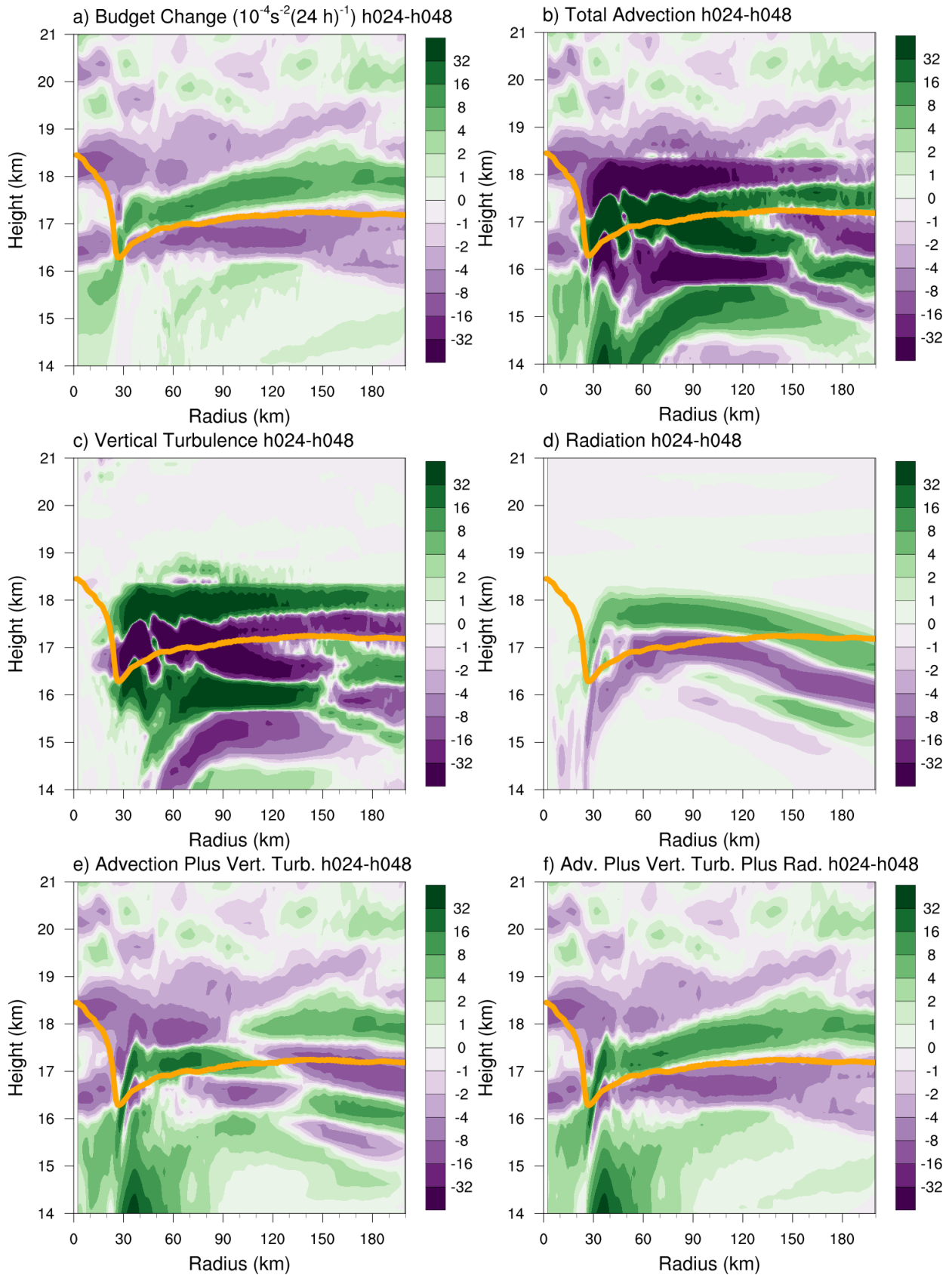


FIG. 6. As in Fig. 5, but for the 24-48-hour period.

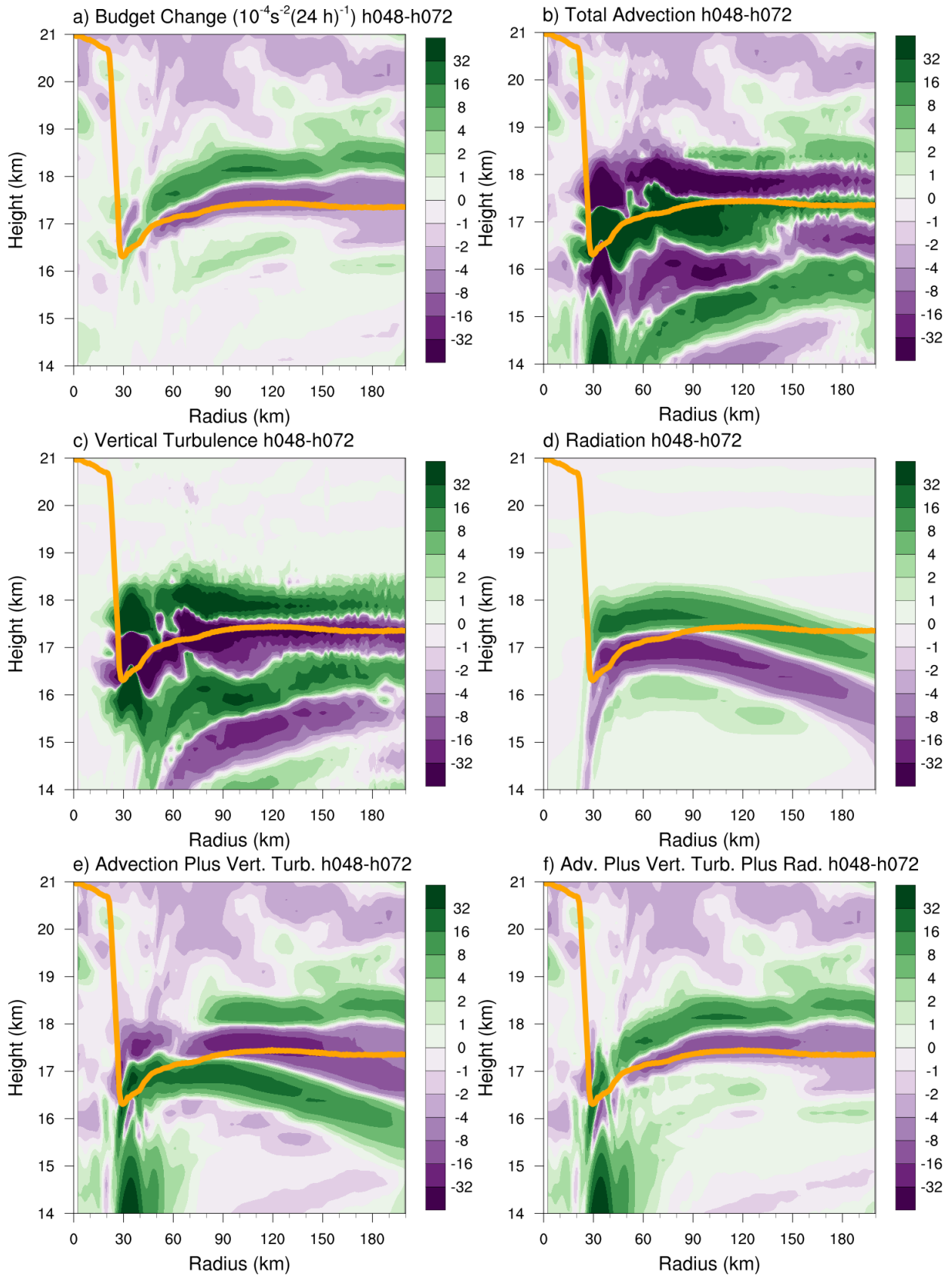


FIG. 7. As in Fig. 5, but for the 48-72-hour period.

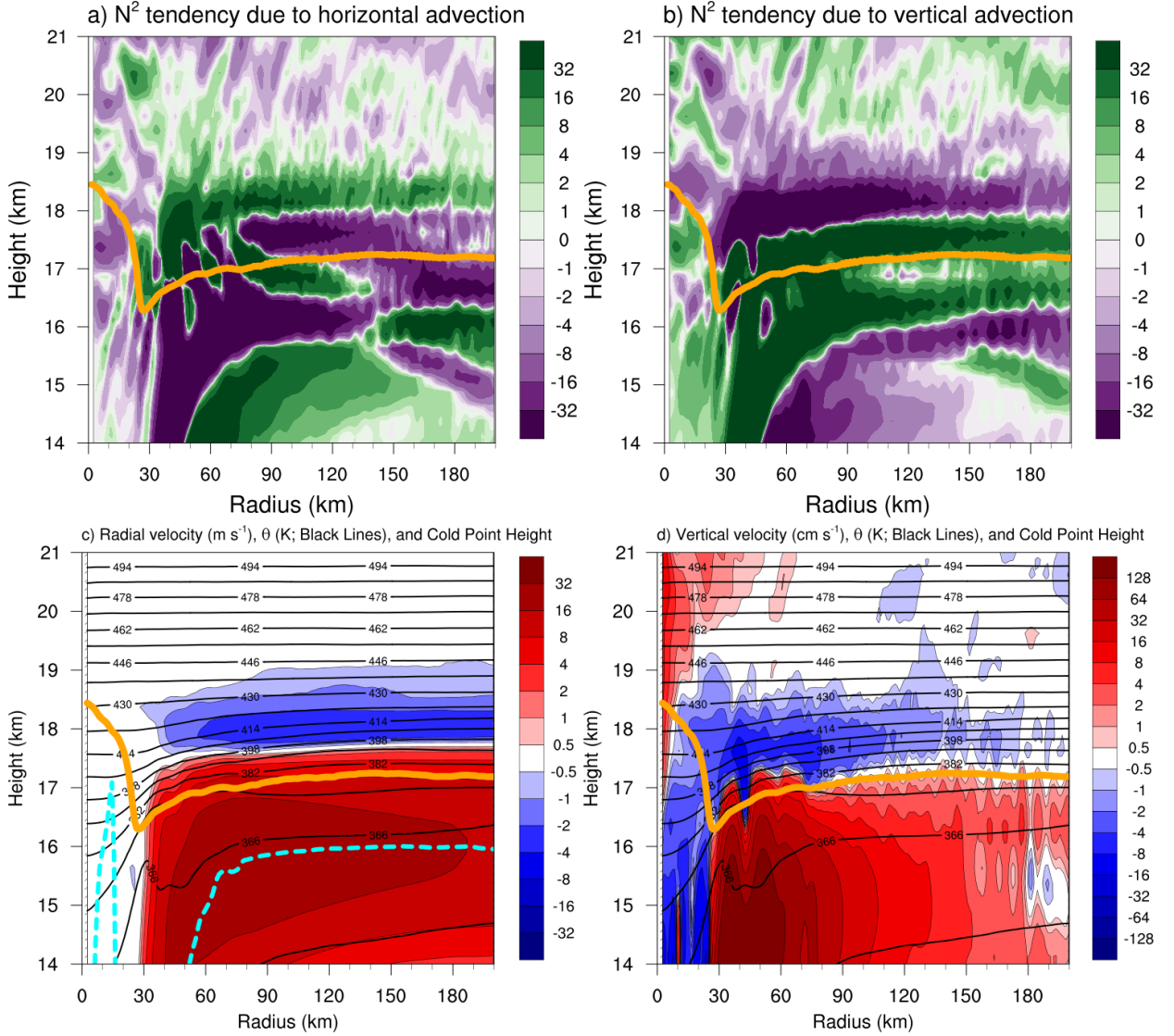
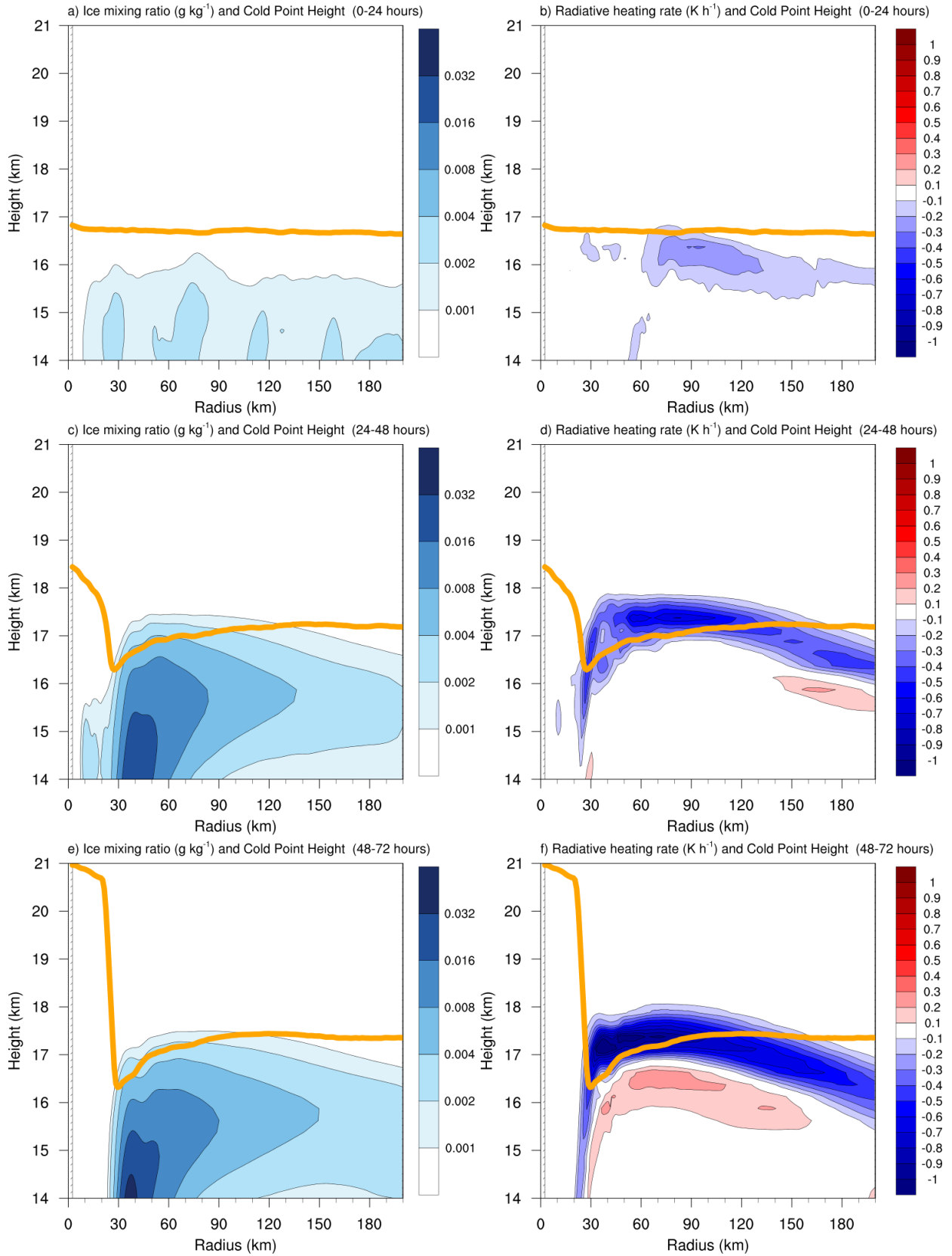


FIG. 8. The contributions to the change in N^2 over the 24-48-hour period ($10^{-4} \text{ s}^{-2} (24 \text{ h})^{-1}$) by (a) horizontal advection and (b) vertical advection. (c) The radial velocity (m s^{-1} ; filled contours), potential temperature (K; thick black contours), cold-point tropopause height (orange line), and level of maximum outflow (dashed cyan line) averaged over the 24-48-hour period. (d) The vertical velocity (cm s^{-1} ; filled contours), potential temperature (K; thick black contours), and cold-point tropopause height (orange line) averaged over the 24-48-hour period.



537 FIG. 9. Ice mixing ratio (g kg^{-1}) and cold-point tropopause height (orange lines) averaged over (a) 0-24 hours,
538 (c) 24-48 hours, and (e) 48-72 hours. Radiative heating rate (K h^{-1}) and cold-point tropopause height (orange
539 lines) averaged over (b) 0-24 hours, (d) 24-48 hours, and (f) 48-72 hours.

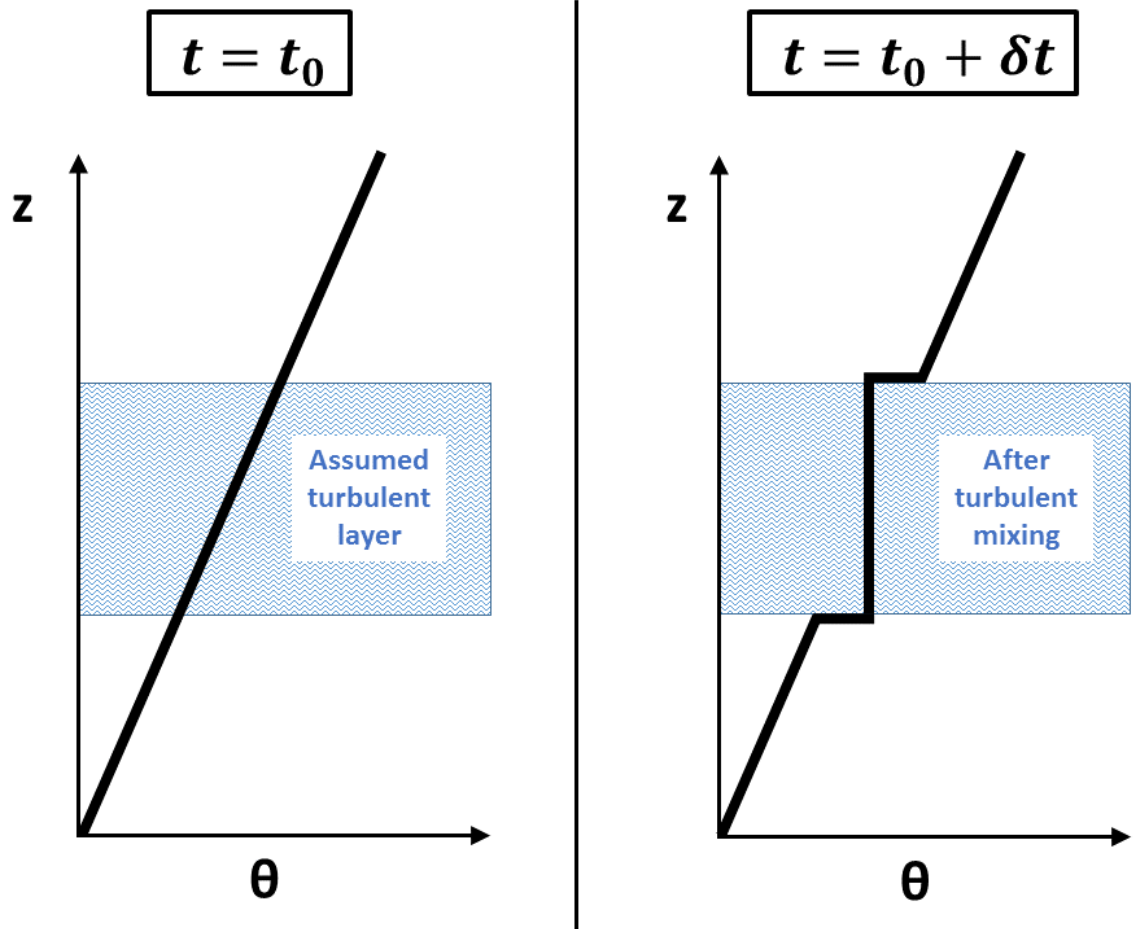


FIG. 10. Schematic diagram of the effect of turbulent mixing on the vertical profile of potential temperature (θ). At the initial time (left panel), potential temperature is assumed to increase with height at a constant rate (thick black line). The imposition of turbulence within a portion of the layer (blue hatching) adjusts the potential temperature profile toward the mean initial value of that layer. After a period of mixing (right panel) the potential temperature in the mixed layer does not vary with height, but just above and just below the mixed layer, it rapidly increases with height.

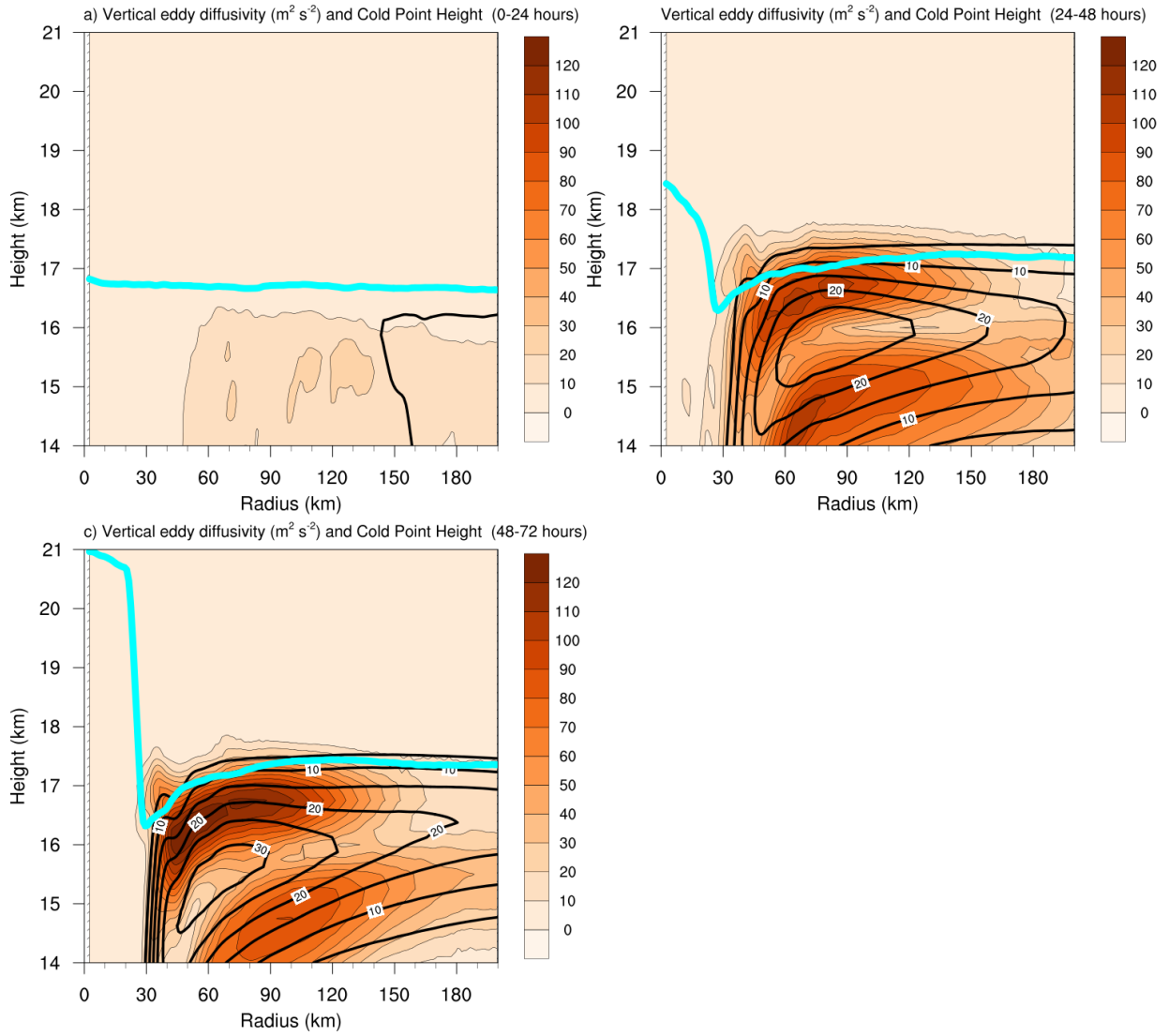
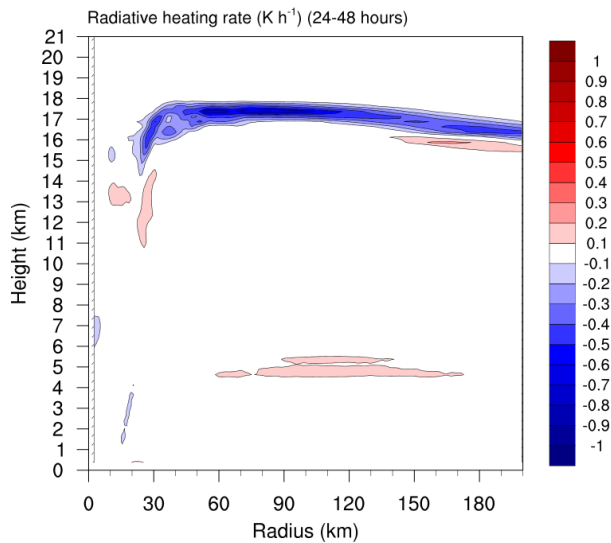
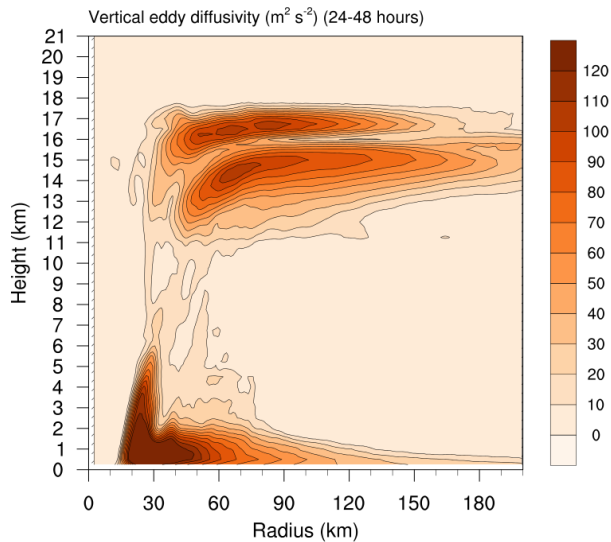
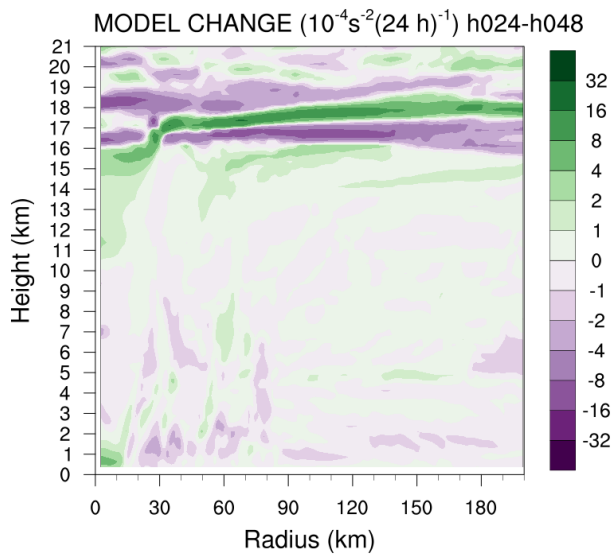


FIG. 11. Vertical eddy diffusivity ($\text{m}^2 \text{s}^{-2}$; filled contours), cold-point tropopause height (cyan lines), and radial velocity (m s^{-1} ; thick black lines) averaged over (a) 0-24 hours, (b) 24-48 hours, and (c) 48-72 hours.



548 FIG. 12. (Top panel) Change in N^2 over the 24-48-hour period ($10^{-4} \text{ s}^{-2} (24 \text{ h})^{-1}$) directly output by the model
549 for the 0-21-km layer. (Middle panel) Vertical eddy diffusivity ($\text{m}^2 \text{ s}^{-2}$) averaged over the same time period.
550 (Bottom panel) Radiative heating rate (K h^{-1}) averaged over the same time period.